Frontiers in Heat and Mass Transfer

Tech Science Press

https://doi.org/10.32604/fhmt.2026.079362

ARTICLE

Experimental Study on the Evaporation Process of Na_2SO_4 Aqueous Solution Droplets under Thermal Radiation Heating

Bingchao Zhao[1,*], Jiahao Yu[1], Zhen Zhang[1], Jinduo Wang[1], Dan Zhang[2] and Wenbo Zhou[2]

[1]College of Energy and Power Engineering, North China University of Water Resources and Electric Power, Zhengzhou, China
[2]School of Energy and Power Engineering, Xi'an Jiaotong University, Xi'an, China

*Corresponding Author: Bingchao Zhao. Email: zhaobingchao@ncwu.edu.cn

Received: 20 January 2026; Accepted: 26 February 2026; Published: 29 June 2026

ABSTRACT: To achieve the goal of deep desalination of saline wastewater driven by solar energy, the evaporation experiments of Na_2SO_4 aqueous solution droplets under thermal radiation heating condition have been carried out with the working conditions of 1450 and 1930 nm, heat flux varied from 1.1×10^5 to 2.5×10^5 W·m^{-2}, initial mass fraction in the range of 0.01~0.16 and droplet initial volume of 2.0~8.0 μL, respectively. The results indicate that absorption coefficient, initial mass fraction, heat flux and initial droplet volume have significantly influences on the evaporation characteristics. The main evaporation time can be shortened by 45.6% and 52% with the growth of the initial mass fraction from 0.01 to 0.16 and the decrease of the initial volume from 8 to 2 μL, respectively. The average evaporation can significantly increase by 55.7% and by 123% with the increase of the initial mass fraction from 0.01 to 0.16 and the heat flux varied from 1.1×10^5 W·m^{-2} to 2.5×10^5 W·m^{-2}, respectively. Moreover, the average evaporation rate of the 1930 nm is 47.7% higher than that of the 1450 nm. Meanwhile, the experimental results have a good agreement with the theoretical values within the relative error in the range of ±30%. In summary, the above results can provide references for the design and engineering application of the desalination system and device of solar salty wastewater.

KEYWORDS: Thermal irradiation; evaporation processes; evaporation rate; absorptivity; crystallization

1 Introduction

With the shortage of global water resources and the increasingly stringent requirements for industrial wastewater discharge, the treatment and resource recovery of saline wastewater are facing major challenges [1,2]. In recent years, the output of Na_2SO_4 waste salt in China is more than 10 million tons [3], and most of these waste salts come from metallurgy, coal chemical industry, printing and dyeing, pesticide, and other industries [4]. The components of these waste salts are complex and accompanied by various harmful substances. Thus, how to effectively treat Na_2SO_4 wastewater becomes particularly urgent and important. At present, the pretreated Na_2SO_4 wastewater is an inorganic salt solution mainly composed of Na_2SO_4. Deep desalination treatment is carried out, that is, the salt and water in the salt solution are completely separated, which can not only reduce environmental pollution, but also recover water to the greatest extent. It is an effective way to solve the above problems [5].

Using solar energy to complete deep desalination is the first choice to reduce processing costs and achieve green production. The existing process of desalination of wastewater by solar heating is mainly based on the efficient absorption of solar energy, and the solution is indirectly heated by heat conduction or convection. In the heat conduction method [6–8], different forms of solid medium provided heat for

the evaporation of salt solution in the form of heat conduction after absorbing solar radiation. However, with the increase of salt concentration, the corrosion of the solid medium was enhanced, and it was difficult to achieve deep desalination. The convection method [9–11] involved heating the air or other gas medium by using solar energy or other heat sources, and then mixing it with the atomized salt solution. The heat was provided to the droplet clusters through convection, and the water vapor produced by the liquid-phase evaporation mixed with the air to form wet steam. Nevertheless, the subsequent separation of these two phases made the process complex and costly. As is well known, both heat conduction and convection methods are surface heating, and their heat transfer efficiency is not very high. Considering that the essence of solar energy is thermal radiation, and the droplet is a semi-transparent medium, the direct heating of salt solution droplets by solar energy can not only improve the heating efficiency, but also omit the heat transfer medium. Therefore, the method of using solar energy can simplify the process and reduce the processing cost. Then, it is necessary to conduct research on the evaporation performance of salt solution droplets under thermal radiation heating conditions.

In order to achieve this goal, the existing research, the research on the thermal radiation absorption performance of droplets with different working fluids is worth learning. Studies have shown that the larger the initial particle size of fuel oil droplets, the more pronounced the enhancement effect of thermal radiation on their evaporation process; thermal radiation can shorten the evaporation time of fuel oil droplets by more than 30% under the condition of large particle sizes. In addition, an exothermic phenomenon occurs during the evaporation of fuel oil droplets, which indicates that the heating power exerts a significant influence on the droplet evaporation rate, and the intrinsic radiation of droplets can further accelerate the evaporation process [12,13]. Research on the evaporation of ethanol droplets under thermal radiation heating has demonstrated that the thermal radiation absorption performance of droplets can be effectively enhanced by adding suitable components or adjusting the concentration of heat-absorbing media inside the droplets [14]. Investigations into the temperature field evolution of kerosene droplets have revealed that for kerosene droplets with a particle size of 2.5 mm, the maximum internal and external temperature difference can reach 55°C at the initial heating stage. With the decrease in droplet particle size, the temperature of droplets gradually tends to be uniform, which suggests that small-sized droplets are gradually transformed into a volumetric heating mode that is more conducive to evaporation [15]. Studies on the temporal evolution of temperature and morphology of droplets on superhydrophobic surfaces under radiation-convection coupling conditions have indicated that the internal temperature of droplets on superhydrophobic surfaces rises first when heated by thermal radiation. Meanwhile, reducing the droplet particle size can significantly increase the evaporation rate by a maximum of 64%, which proves that decreasing the particle size is an effective approach to accelerate the droplet evaporation process [16]. Research on the heating and evaporation of single water droplets has shown that the introduction of thermal radiation can increase the evaporation rate of water droplets by 23% and raise the saturation temperature by 5°C. It is thus evident that thermal radiation heating can effectively enhance the evaporation rate and saturation temperature of droplets to achieve rapid droplet evaporation [17]. Relevant studies have further pointed out that the thermal radiation absorption performance of droplets is closely related to their volume and shape [18]. Research on the evaporation of n-decane and diesel droplets under thermal radiation heating has found that the average absorption coefficient of diesel is 3.9×10^5 m^{-1}, which is much higher than that of n-decane (3.8×10^4 m^{-1}). Under the same conditions, the evaporation time of diesel droplets is approximately 30% shorter than that of n-decane droplets, which demonstrates that the absorption coefficient is a key factor affecting the heating and evaporation of diesel droplets [19]. Research on n-dodecane and pure water droplets under the combined heating of radiation and convection has shown that both the temperature and evaporation rate of the droplets exhibit a non-monotonic variation of increasing first and then decreasing. In the early

stage of evaporation, the heat required for droplet evaporation is mainly provided by convection, while in the late stage of evaporation, the heat is mainly derived from the external irradiation energy absorbed and accumulated by the droplets [20]. The evaporation evolution of pure water droplets can be divided into two stages: heating and evaporation. The diameter of pure water droplets remains almost unchanged during the heating stage, whereas the variation of droplet diameter in the evaporation stage deviates significantly from the classical D^2 law [21,22]. Investigations into the radiative transfer processes (including absorption and scattering) of single pure water droplets and droplet clusters have revealed that the thermal radiation absorption modes of heated droplets can be classified into volumetric absorption and surface absorption. When volumetric absorption dominates, increasing the absorption coefficient or refractive index of droplets can simultaneously improve their heating rate and absorption efficiency. The reduction in droplet particle size leads to a rapid decrease in the overall absorption rate of external radiation by droplets, as a large portion of incident radiation escapes in the form of scattering. Therefore, the overall absorption rate of the droplet system can be improved by rationally arranging droplet clusters based on the spatial distribution of scattered radiation [23–25].

In summary, the existing research on the thermal radiation absorption performance of droplets has primarily focused on working fluids such as water, fuel, and organic solvents, while studies on Na_2SO_4 aqueous solution droplets are relatively scarce. Given that the near-infrared spectral characteristics of Na_2SO_4 aqueous solution are similar to those of pure water, which exhibits absorption peaks at 1450 and 1930 nm, this study establishes a single-droplet experimental system for thermal radiation heating [26–28]. Using Na_2SO_4 aqueous solution droplets as the subject, and employing infrared lasers at its preferential absorption bands of 1450 and 1930 nm as the radiation source, we conduct a systematic experimental investigation into the characteristics of the droplet evaporation process under thermal radiation heating.

2 Experimental System

2.1 Experimental System and Experimental Procedures

The experimental system of single droplet heating under thermal radiation conditions is conducted in Fig. 1. The system mainly consists of laser emitter, data acquisition system, thermocouples, droplet suspension bracket, laser lens and high-speed camera. The main parameters and several key measurement instruments of the experimental system are provided in Table 1. Each working condition of the experiment was conducted three times. The detailed procedural timeline is provided in Fig. 2.

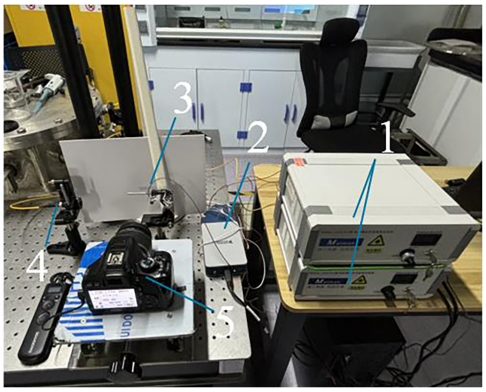

Figure 1: Na_2SO_4 droplet evaporation experiment system. 1—Laser emitter; 2—Data acquisition system; 3—Thermocouples and droplet suspension bracket; 4—Laser lens; 5—High speed camera.

Table 1: Main parameters of the experimental system.

Experimental Equipment	Model	Range
Na_2SO_4 crystal	DINGSHENGXIN	Purity: 0.995
Humidity and Temperature Meter	VICTOR231	Temperature: −25.0°C~75.0°C (±0.3°C) Ambient temperature: 20.0°C~23.0°C Humidity: 0%~99.9% RH (±2% RH) Ambient humidity: 16.0%~20.0% RH
CCD	Canon 550D	Pixel: 3250 × 782 pixels
Laser 1450	NMDL-1450-2.0	Wavelength: 1450 nm Power: 0–1.8 W Spot diameter: 3 mm
Laser 1930	NMDL-1930-0.8	Wavelength: 1930 nm Power: 0–0.8 W Spot diameter: 1 mm
Concentration titrator Pipette gun Thermocouple Camera lens	WDDY-3000 UCHEN T EF 50 mm f/1.0 L USM	Concentration: 0~26 g/L (±0.01 g/L) Volume: 0.5~10 μL (0.1 μL) Temperature: −200°C~400°C (±0.5°C) Focal length: 50 mm

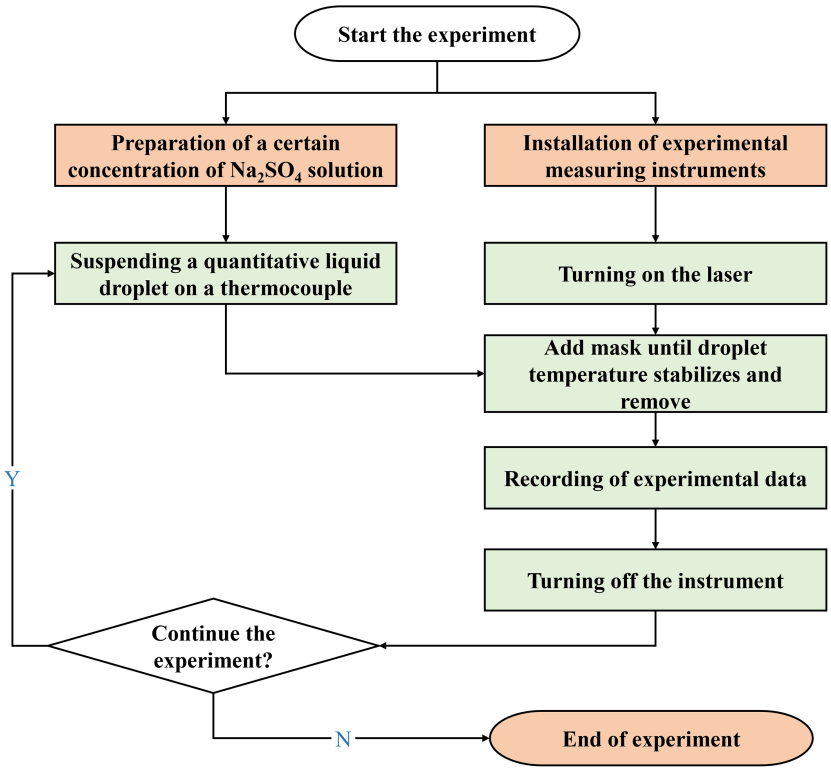

Figure 2: The diagram of Na_2SO_4 droplet evaporation experiment procedure.

The droplet profile captured during the experiment is shown in Fig. 3a. Based on the experimental images, by programming to identify the pixel points and gray values in the images, the major axis a, minor axis b of the droplets in the images and the volume V_r of the thermocouple can be obtained, as illustrated in Fig. 3b. According to the volume calculation formula of an ellipsoid, the equivalent diameter d of the droplet is derived using Eq. (1), and the change in this diameter is used to characterize the droplet's heating and evaporation process. The equivalent diameter measurement method adopted in this study is similar to that reported in Reference [29], where the droplet is assumed to be an ellipsoid and the diameter value is converted using the ellipsoid volume formula.

$$d = \sqrt[3]{\frac{8\pi ab^2 - 6V_r}{\pi}} \tag{1}$$

where d/mm is the droplet diameter, a/mm is the droplet major axis, b/mm is the droplet minor axis, and V_r/mm^3 is the thermocouple volume.

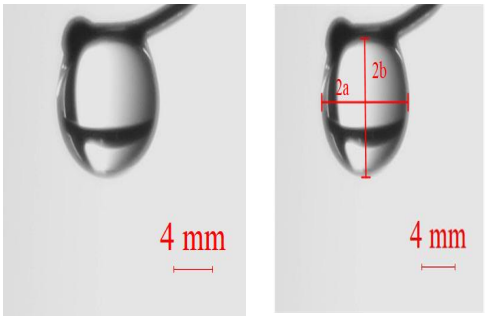

Figure 3: Schematic diagram of digital processing of Na_2SO_4 droplet images. (**a**) Experimental photographs; (**b**) Post-processing pictures.

2.2 Uncertainty Analysis

Table 2 presents the parameter ranges of the experiments in this study and the results of uncertainty analysis for the main measured parameters, where the uncertainty was evaluated in accordance with the Constant Odds Combination method proposed by Moffat [30].

Table 2: The uncertainty of experimental parameters.

Main Parameters	Range	Absolute Error	Minimum Measured Value	Uncertainties
$f_{m,0}$/1	0.01~0.16	0.0004	0.01	4%
V_0/μL	2.0~8.0	0.04	2.0	2%
t/°C	20~120	0.3	20	1.5%
d/mm	1.56~2.48	3.2×10^{-3}	1.56	0.2%
K_{ab}/K·s^{-1}	0.65~5.33	0.02	0.65	3.1%
q_b/W·m^{-2}	1.1~2.5 × 10^5	0.3 × 10^4	1.1 × 10^5	2.7%
$\dot{m}$/kg·s^{-1}	2.33~8.33 × 10^{-8}	0.1 × 10^{-9}	2.33 × 10^{-8}	0.4%

3 Results and Discussion

This study conducted a systematic experimental investigation on the evaporation characteristics of Na_2SO_4 aqueous solution droplets with respect to multiple key parameters, including heat flux, wavelength, initial mass fraction of the droplet, and initial volume of the droplet.

3.1 Droplet Evaporation Process

Fig. 4 illustrates the evaporation process of Na_2SO_4 aqueous solution droplets with different initial mass fractions under a heat flux of $q_b = 2.5 \times 10^5$ W·m^{-2}. It can be observed that: (1) For Case 1 (pure water droplet), the droplet volume continuously decreases over time and eventually evaporates completely. (2) With the increase in initial mass fraction, the evaporation of Na_2SO_4 solution droplets (taking Case 4 as an example) undergoes multiple stages: Within 0~15 s: The droplet volume gradually decreases due to water evaporation, and the solution is continuously concentrated; During 15~20 s: Crystals begin to precipitate on the droplet surface, and subsequently grow rapidly to cover the entire droplet surface, forming a closed crystal shell; Within 20~40 s: The volume of the droplet enclosed in the crystal shell no longer decreases, but slightly expands due to the internal vapor, and is eventually completely dried out.

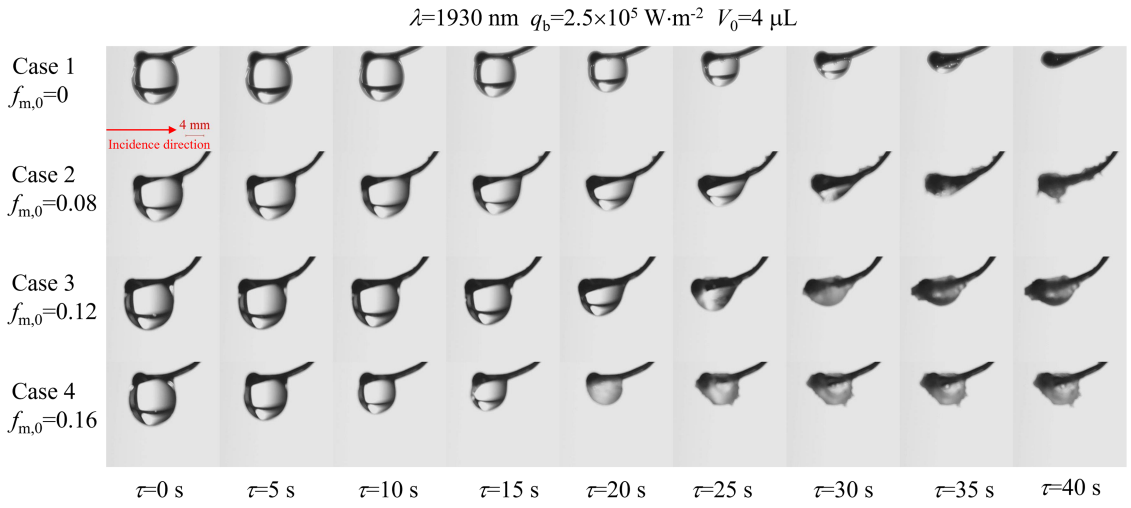

Figure 4: Visualization study on droplet evaporation morphology under different initial mass fractions.

Fig. 5 illustrates the variation law of droplet temperature and diameter with time. Based on this, the evaporation process of Na_2SO_4 aqueous solution droplets can be divided into four stages: (1) Temperature rise stage (ab segment): The droplet temperature rises rapidly with a slight decrease in volume; (2) Crystallization stage (bc segment): The droplet continuously evaporates at an approximately constant temperature, with the volume further decreasing. Crystals begin to precipitate on its surface and gradually cover the entire droplet; (3) Thermal expansion stage (cd segment): Since the surface crystal shell hinders the evaporation and escape of internal water, vapor accumulation causes the droplet to expand, and the temperature rises again simultaneously; (4) Temperature drop stage (de segment): At this point, the internal water of the droplet has completely evaporated, and the crystal shell stops expanding.

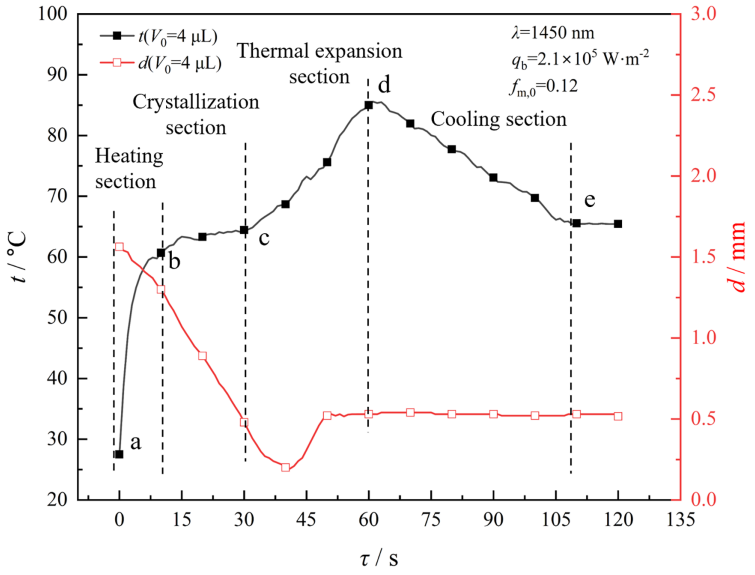

Figure 5: The variation laws of droplet evaporation temperature and particle size over time.

3.2 Heating Section and Temperature Rise Rate

If the end time of the temperature rise period is defined as the moment when the absolute value of the droplet temperature change rate $|\partial t/\partial \tau|$ first drops below 1 K·s^{-1}, the average temperature rise rate of this stage can be calculated by Eq. (2):

$$K_{ab} = \frac{t_b - t_a}{\tau_{ab}} \tag{2}$$

where t_b/°C is the end temperature of the temperature rise period; t_a/°C is the initial droplet temperature; and τ_{ab}/s is the duration of the Heating section.

Fig. 6 compares the relationship between the temperature rise rate K_{ab} of the temperature rise period and the initial droplet mass fraction $f_{m,0}$ under different initial volumes, heat fluxes, and wavelengths. In Fig. 6a, K_{ab} shows an overall increasing trend with the increase in $f_{m,0}$. Taking $f_{m,0}$ = 0.05 as an example, when q_b increases from 1.1 × 10^5 W·m^{-2} to 2.5 × 10^5 W·m^{-2}, the corresponding K_{ab} increases from 1.4 to 3.3 K·s^{-1}; for each increase of 0.3 × 10^5 W·m^{-2} in q_b, the increase range of K_{ab} is between 0.8–1.0 K·s^{-1}. In Fig. 6b, under the same $f_{m,0}$ and V_0, K_{ab} increases with the increase in the droplet absorption coefficient, and the optical thickness of the droplets is all greater than 1, indicating that the droplets absorb thermal radiation through surface absorption in the experiment. Taking V_0 = 2 μL and $f_{m,0}$ = 0.05 as an example, the K_{ab} values corresponding to 1450 and 1930 nm are 2.1 and 2.4 K·s^{-1}, respectively, representing an increase of 14%. With $f_{m,0}$ kept constant, K_{ab} increases as the initial droplet volume V_0 decreases. Taking λ = 1450 nm and $f_{m,0}$ = 0.05 as an example, when V_0 decreases from 8 to 2 μL, K_{ab} increases from 1.2 to 2.1 K·s^{-1}, an increase of 83%. This is because the decrease in initial droplet volume reduces both the light-receiving area and the mass of the droplet, but the reduction amplitude of the light-receiving area is smaller than that of the mass. Therefore, the energy absorbed per unit mass increases, leading to an improvement in the temperature rise rate.

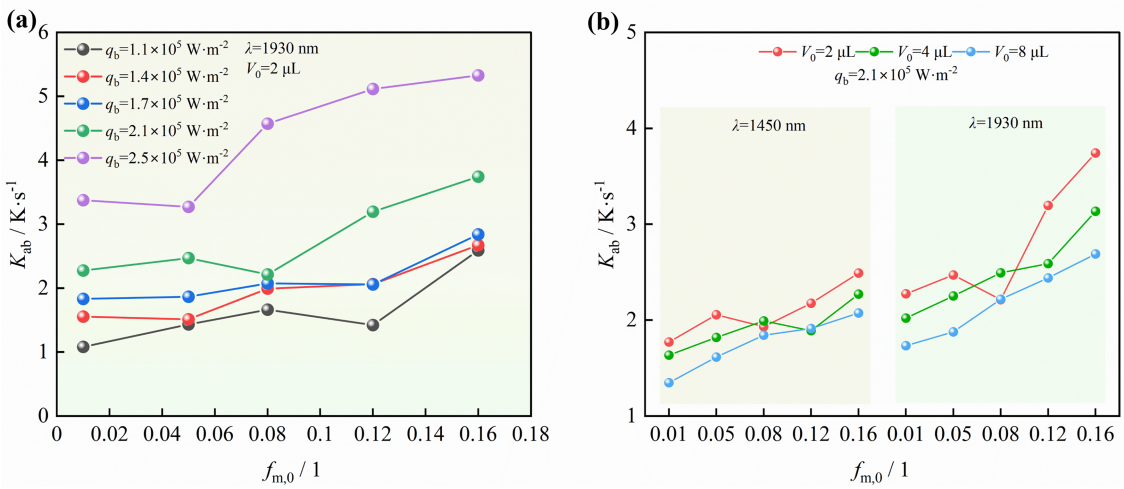

Figure 6: The variation law of the heating rate with the initial mass fraction of the droplet. (**a**) The change rule of heating rate under different heat flux density; (**b**) The change law of heating rate under different initial volume and incident wavelength.

3.3 Crystallization Section and Crystallization Duration

Figs. 7 and 8 respectively illustrate the variation relationships between the crystallization temperature t_m, crystallization duration τ_{bc}, and the initial droplet mass fraction $f_{m,0}$ under different initial volumes, heat fluxes, and wavelengths. In Fig. 7a, t_m shows an overall increasing trend with the increase in $f_{m,0}$ and q_b. Under the condition of $q_b = 1.7 \times 10^5$ W·m^{-2}, t_m increases from 49°C to 54°C (an increase of 5°C) with the change in the initial droplet mass fraction. This is because the saturated vapor pressure on the droplet surface decreases, leading to an increase in the crystallization temperature t_m required for stable evaporation and crystallization. In Fig. 7b, under the same $f_{m,0}$, t_m increases with the increase in the initial droplet volume or droplet absorption coefficient. In Fig. 8a, the increase in $f_{m,0}$ accelerates the precipitation of Na_2SO_4, resulting in an approximately linear decrease in τ_{bc} with the increase in $f_{m,0}$. Under the condition of $q_b = 1.7 \times 10^5$ W·m^{-2}, the corresponding τ_{bc} decreases from 68 to 33 s (a reduction of 51%) with the change in the initial droplet mass fraction. In Fig. 8b, under the same $f_{m,0}$, τ_{bc} shortens with the increase in the initial droplet volume or droplet absorption coefficient. Under the conditions of λ = 1450 nm and $f_{m,0}$ = 0.05, τ_{bc} decreases from 112 to 54 s as the initial volume decreases; under the conditions of $f_{m,0}$ = 0.05 and V_0 = 2 μL, τ_{bc} is reduced by 14 s. The above results indicate that increasing the heat flux, reducing the initial droplet volume, or selecting a wavelength with a larger droplet absorption coefficient can all promote faster crystallization of the droplets.

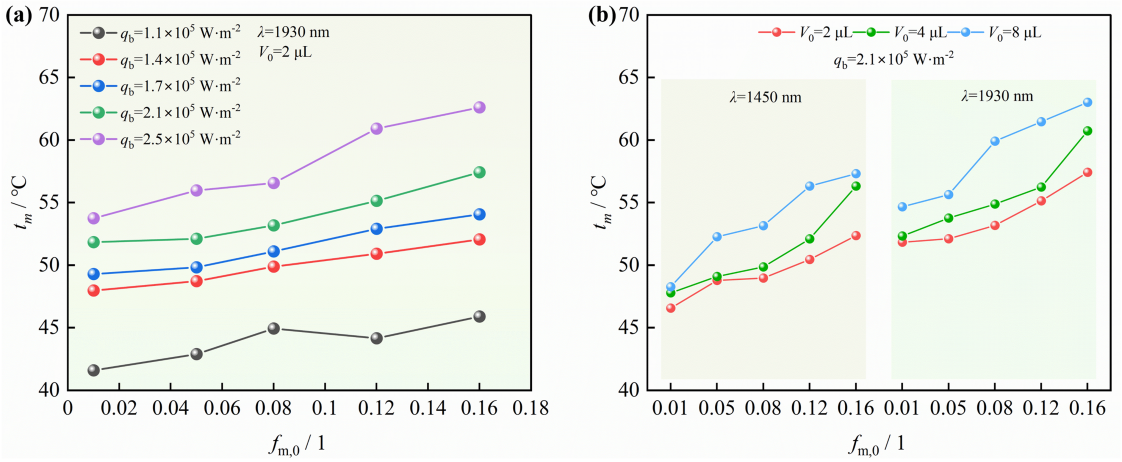

Figure 7: The variation law of crystallization temperature with the initial mass fraction of the droplet. (**a**) The change rule of crystallization temperature under different heat flux density; (**b**) The variation law of crystallization temperature under different initial volume and incident wavelength.

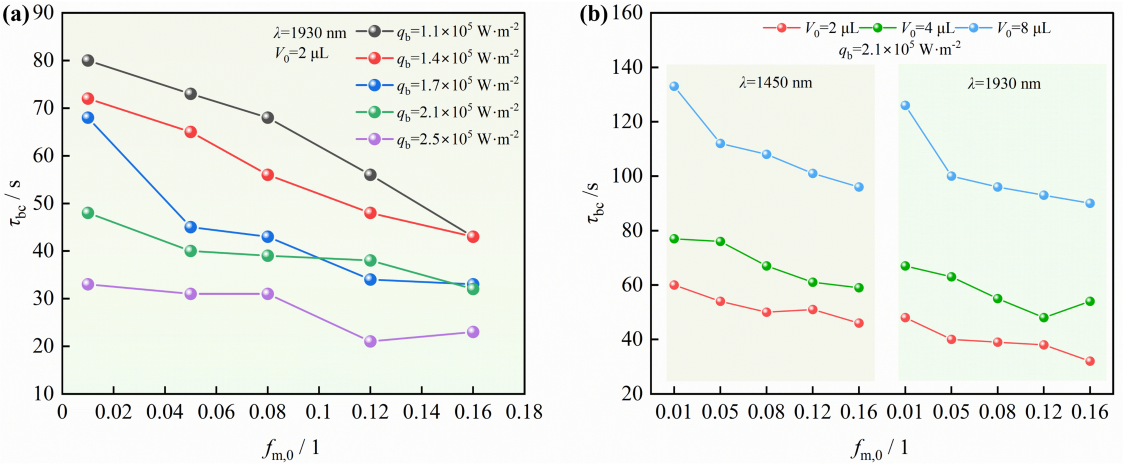

Figure 8: The variation law of crystallization time with the initial mass fraction of the droplet. (**a**) The change rule of crystallization time under different heat flux density; (**b**) The change rule of crystallization time under different initial volume and incident wavelength.

3.4 Maximum Temperature and Duration of the Thermal Expansion Section

Figs. 9 and 10 respectively compare the relationships between the thermal expansion duration τ_{cd}, maximum temperature t_{max}, and the initial droplet mass fraction $f_{m,0}$ under different initial volumes, heat fluxes, and wavelengths. In Fig. 9a, t_{max} shows an overall increasing trend with the increase in heat flux and mass fraction. This is because as evaporation proceeds continuously, the droplet has a higher salt content and a thicker crystal shell, making the evaporation and escape of internal residual water more difficult, thus leading to an increase in t_{max}. In Fig. 9b, t_{max} increases with the increase in the initial droplet volume or absorption coefficient. In Fig. 10a, τ_{cd} shortens with the increase in heat flux and initial mass fraction. In Fig. 10b, τ_{cd} shortens as the initial volume decreases. Under the conditions of λ = 1450 nm and $f_{m,0}$ = 0.05, τ_{cd} is shortened by 50% with the decrease in volume; τ_{cd} also shortens with the increase in absorption coefficient, and under the conditions of $f_{m,0}$ = 0.05 and V_0 = 2 μL, τ_{cd} decreases from 26 to 14 s.

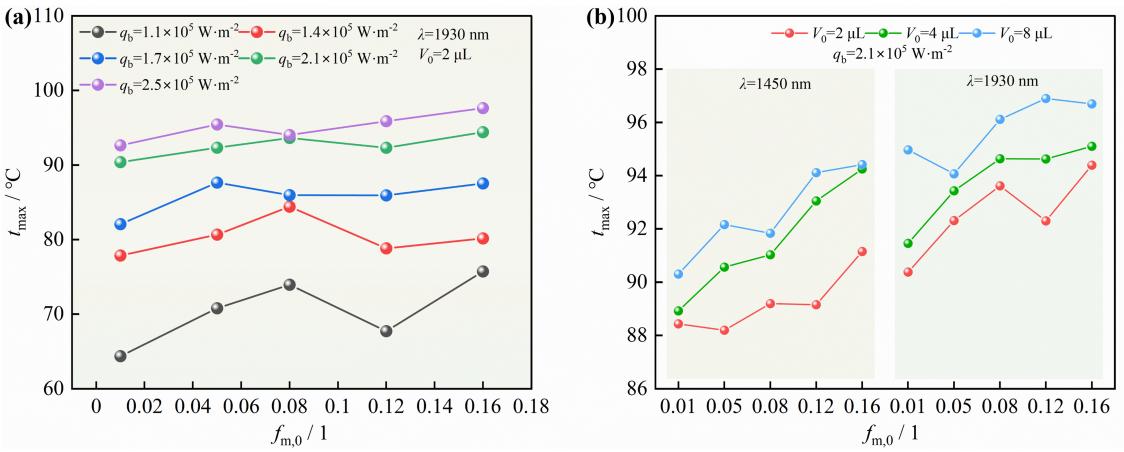

Figure 9: The variation law of the maximum temperature with the initial mass fraction of the droplet. (**a**) The maximum temperature change rule under different heat flux density; (**b**) The maximum temperature variation law under different initial volume and incident wavelength.

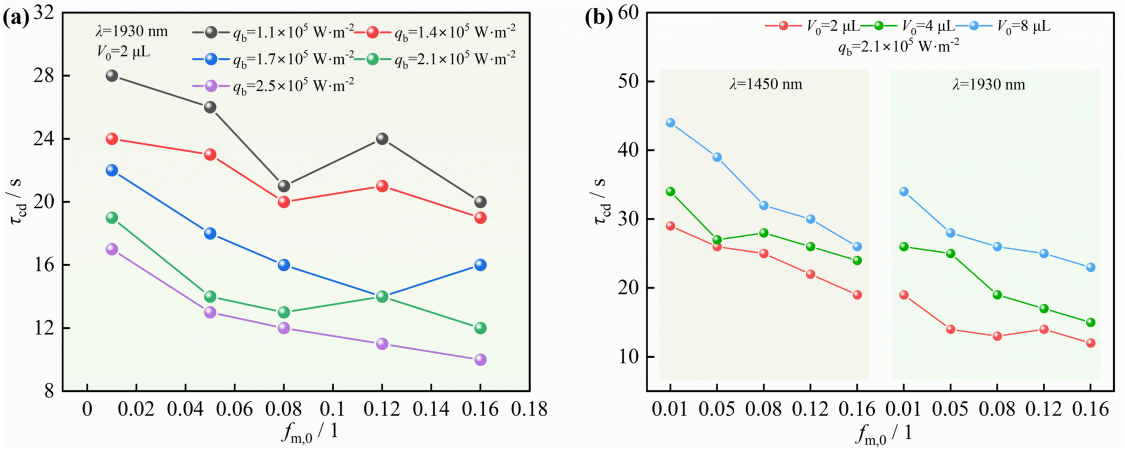

Figure 10: The variation law of the thermal expansion period with the initial mass fraction of the droplet. (**a**) The change rule of thermal expansion time under different heat flux density; (**b**) The variation law of thermal expansion time under different initial volume and incident wavelength.

3.5 Average Evaporation Rate of the Droplet Surface

The crystallization period and thermal expansion period are the main stages of droplet evaporation. Based on this, the average evaporation rate of the droplet surface is defined as the mass of water evaporated from the droplet during the time period τ_{bd}, and its calculation formula is given by Eq. (3) below:

$$m_{Exp} = \frac{\rho_b V_0 (1 - f_{m,0})}{\tau_{bd}} \tag{3}$$

where ρ_b/kg·m^{-3} is the density of the droplet in the initial state; V_0/μL is the initial volume of the droplet; $f_{m,0}$/1 is the initial mass fraction of the droplet; and τ_{bd}/s is the total duration of the crystallization section and thermal expansion section.

Fig. 11 compares the variation of the average evaporation rate m_{Exp} of the droplet surface with the initial mass fraction $f_{m,0}$ under different initial volumes, heat fluxes, and wavelengths. In Fig. 11a, $\dot{m}$ shows an

overall increasing trend with the increase in $f_{m,0}$ and q_b. Under the condition of q_b = 1.7 × 10^5 W·m^{-2}, as $f_{m,0}$ increases, m_{Exp} rises from 2.73 × 10^{-8} kg·s^{-1} to 4.25 × 10^{-8} kg·s^{-1}, representing an increase of 55.7%. In Fig. 10b, using a wavelength with a large absorption coefficient or increasing the initial droplet volume can improve m_{Exp}. Under the conditions of λ = 1450 nm and $f_{m,0}$ = 0.05, as the initial volume increases, m_{Exp} increases from 2.95 × 10^{-8} kg·s^{-1} to 6.24 × 10^{-8} kg·s^{-1}, an increase of 111.5%; under the conditions of V_0 = 2 μL and $f_{m,0}$ = 0.05, the increase in $\dot{m}$ reaches 47.7% with the increase in the absorption coefficient. The above results indicate that increasing the external radiation power, using a wavelength with a large absorption coefficient, or increasing the initial droplet volume can simultaneously increase the crystallization temperature and the maximum temperature of the thermal expansion period, i.e., increasing the average temperature level during the droplet evaporation process. Meanwhile, m_{Exp} increases accordingly, meaning that the droplet temperature is the main factor affecting m_{Exp}.

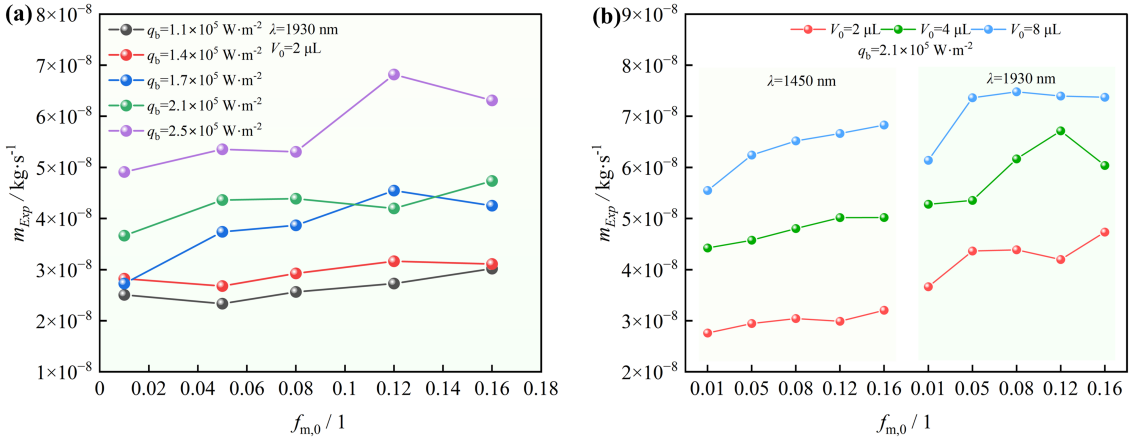

Figure 11: The variation law of the average surface evaporation rate with the initial mass fraction of the droplet. (**a**) The variation law of surface average evaporation rate under different heat flux density; (**b**) The variation law of the average evaporation rate of the surface under different initial volume and incident wavelength.

The experimental values calculated from Eq. (3) are compared with the theoretical values of the average evaporation rate of the droplet surface from Eq. (4) reported in Reference [24]. As shown in Fig. 12, the relative errors are within ±30%.

$$m_{Cal} = \pi d \rho_g \cdot D \cdot Sh \cdot \ln(1 + B_M) \tag{4}$$

in which;

$$t_p = \frac{q_b \cdot d \cdot [1 - \exp(-\kappa d)]}{\lambda_b \cdot (1.176 f_{m,0} + 1.323)} \tag{5}$$

$$Sh = \frac{h_m d}{D} = 2 + 0.552 \mathrm{Re}^{0.5} Sc_g^{0.33} \tag{6}$$

$$\mathrm{Re} = \frac{d \cdot u}{\nu_g} \tag{7}$$

$$Sc_g = \frac{\nu_g}{D} \tag{8}$$

$$B_M = \frac{Y_{v,s} - Y_{v,a}}{1 - Y_{v,s}} \tag{9}$$

$$D = 1.482 \times 10^{-5} \left(\frac{t_p^{1.936}}{p} \right) \tag{10}$$

where B_M/1 is the Spalding mass transfer number; $Y_{v,s}$/1 is the vapor mass fraction at the droplet surface; $Y_{v,a}$/1 is the vapor mass fraction in the environment; D/m^2·s^{-1} is the diffusion coefficient; t_p/K is the qualitative temperature of the droplet; and λ_b/W·m^{-1}·K^{-1} is the thermal conductivity.

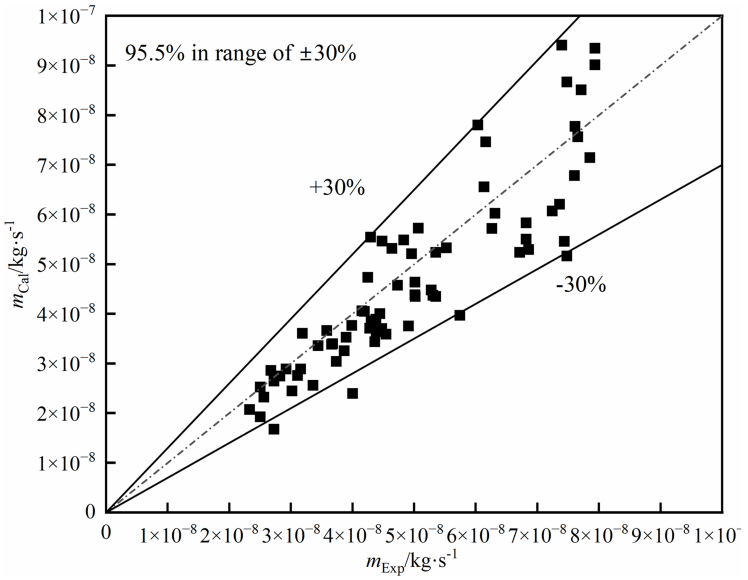

Figure 12: The relative error between the experimental and theoretical values of the average evaporation rate on the surface of Na_2SO_4 droplets.

4 Conclusions

In this study, a thermal radiation-heated single droplet experimental system was established, and experimental research was conducted on the evaporation process of Na_2SO_4 aqueous solution droplets under thermal radiation. The main conclusions are as follows:

(1) Under thermal radiation heating, the evaporation process of Na_2SO_4 aqueous solution droplets is jointly affected by external parameters such as heat flux and radiation wavelength, as well as internal parameters including initial droplet mass fraction and initial volume. Based on the evolutionary characteristics of droplet temperature and diameter, the process can be divided into four stages: temperature rise period, crystallization period, thermal expansion period, and temperature drop period. Among these, the crystallization period and thermal expansion period are the main stages of droplet evaporation.

(2) Using a wavelength with a high absorption coefficient, reducing the initial droplet volume, increasing the heat flux, or enhancing the initial mass fraction can all effectively improve the overall radiation absorption capacity and evaporation performance of the droplets. Compared with radiation at 1450 nm, using radiation at 1930 nm can increase the average temperature rise rate by 88% and the average evaporation rate by 47.7%. When the initial droplet volume decreases from 8 to 2 μL, the duration of the main evaporation period is shortened by 52%. As the heat flux increases from 1.1 × 10^5 W·m^{-2} to 2.5 × 10^5 W·m^{-2}, the main evaporation period is reduced by 55.5%, and the average evaporation rate is increased by 129%. Meanwhile, increasing the initial mass fraction from 0.01 to 0.16 shortens the main evaporation period by 45.6% and improves the average evaporation rate by 55.7%.

(3) The experimentally calculated values of the average evaporation rate of the droplet surface range from 2.33×10^{-8} to 8.33×10^{-8} kg·s^{-1}, with relative errors between the experimental and theoretical values within ±30%. This study can provide a reference for the design and engineering application of solar thermal radiation-based saline wastewater desalination systems.

Acknowledgement: Sincere gratitude is extended to North China University of Water Resources and Electric Power for providing an excellent academic and research environment that has significantly facilitated the completion of this work. The university's well-equipped facilities, supportive academic atmosphere, and dedication to fostering research innovation have been invaluable throughout the entire research process.

Funding Statement: The authors gratefully acknowledge the financial support of Henan Province Science and Technology Research Project (No. 252102320101), the National Natural Science Foundation of China (No. 51976162 and No. 52206012) and the Advanced Talents Research Start-up Project of North China University of Water Resources and Electric Power (201611030).

Author Contributions: Bingchao Zhao: Methodology, writing—original draft preparation, funding acquisition, project administration; Jiahao Yu: Investigation, formal analysis, data curation; Zhen Zhang: Supervision, formal analysis; Jinduo Wang: Investigation, formal analysis; Dan Zhang: Conceptualization, funding acquisition; Wenbo Zhou: Supervision, formal analysis. All authors reviewed and approved the final version of the manuscript.

Availability of Data and Materials: The authors confirm that the data supporting the findings of this study are available within the article.

Ethics Approval: Not applicable.

Conflicts of Interest: The authors declare no conflicts of interest.

Nomenclature

a	Long axis of droplet (mm)
b	Droplet short axis (mm)
B_M	Spalding mass transfer number
d	Equivalent diameter of droplet (mm)
D	Diffusion coefficient (m^{-2}·s^{-1})
$f_{m,0}$	Droplet mass fraction of Na_2SO_4 aqueous solution
h_m	Droplet heat transfer coefficient (W·m^{-2}·K^{-1})
K_{ab}	Heating rate of heating section (K·s^{-1})
$\dot{m}$	Average surface evaporation rate (kg·s^{-1})
p	Ambient pressure (Pa)
q_b	Heat flux density (W·m^{-2})
Re	Reynolds number
Sc	Schmidt number
Sh	Sherwood number
t	Droplet temperature (°C)
t_0	Ambient temperature (K)
t_a	Initial droplet temperature (°C)
t_b	End temperature of droplet heating section (°C)
t_c	End temperature of droplet crystallization section (°C)
t_d	End temperature of droplet thermal expansion section (°C)
t_m	Droplet crystallization temperature (°C)
t_{max}	Maximum droplet temperature (°C)

t_p	Droplet qualitative temperature (K)
u_g	Air flow velocity ($m \cdot s^{-1}$)
V_0	Initial volume of droplet (μL)
V_r	Thermocouple volume (mm^3)
v_g	Viscosity coefficient of motion ($m^{-2} \cdot s^{-1}$)
$Y_{v,a}$	The mass fraction of steam in the surrounding environment
$Y_{v,s}$	Steam mass fraction on droplet surface
κ	Absorption coefficient (m^{-1})
λ	Wave length (nm)
λ_b	Thermal conductivity ($W \cdot m^{-1} \cdot K^{-1}$)
μ_g	Dynamic viscosity (Pa·s)
ρ_b	The density of droplets in the initial state ($kg \cdot m^{-3}$)
ρ_g	Air density ($kg \cdot m^{-3}$)
τ	Evaporation time (s)
τ_{ab}	The duration of droplet heating section (s)
τ_{bc}	Duration of droplet crystallization section (s)
τ_{cd}	The duration of droplet thermal expansion section (s)

References

1. Marinova S, Bach V, Link A, Finkbeiner M. Criticality assessment of global freshwater resource use: adapting abiotic resource criticality frameworks—Water SCARCE. Sci Total Environ. 2025;966:178676. doi:10.1016/j.scitotenv.2025.178676.
2. Karimidastenaei Z, Avellán T, Sadegh M, Kløve B, Haghighi AT. Unconventional water resources: global opportunities and challenges. Sci Total Environ. 2022;827:154429. doi:10.1016/j.scitotenv.2022.154429.
3. Huang L, Wang D, He C, Pan M, Zhang B, Chen Q, et al. Industrial wastewater desalination under uncertainty in coal-chemical eco-industrial parks. Resour Conserv Recycl. 2019;145(7):370–8. doi:10.1016/j.resconrec.2019.02.036.
4. Feng L, Tian B, Zhu M, Yang M. Current progresses in the analysis, treatment and resource utilization of industrial waste salt in China: a comprehensive review. Resour Conserv Recycl. 2025;217:108224. doi:10.1016/j.resconrec.2025.108224.
5. Zheng JG, Zhang D, Yuan Y, Wang YX, Yang QZ. Numerical simulation of aqueous NaCl in parallel hot air mixing and spray flashing within finite rectangle tube. J Xi'an Jiaotong Univ. 2023;57(2):173–83. Available from: https://link.cnki.net/urlid/61.1069.T.20220928.1505.004.
6. Chen Q, Burhan M, Shahzad MW, Ybyraiymkul D, Akhtar FH, Li Y, et al. A zero liquid discharge system integrating multi-effect distillation and evaporative crystallization for desalination brine treatment. Desalination. 2021;502:114928. doi:10.1016/j.desal.2020.114928.
7. Hsieh CC, Yao SC. Evaporative heat transfer characteristics of a water spray on micro-structured silicon surfaces. Int J Heat Mass Transf. 2006;49(5–6):962–74. doi:10.1016/j.ijheatmasstransfer.2005.09.013.
8. Aly S, Jawad J, Manzoor H, Simson S, Lawler J, Mabrouk AN. Pilot testing of a novel integrated Multi Effect Distillation—Absorber compressor (MED-AB) technology for high performance seawater desalination. Desalination. 2022;521:115388. doi:10.1016/j.desal.2021.115388.
9. Bai BF, Zhang HB, Liu L, Sun HJ. Experimental study on turbulent mixing of spray droplets in crossflow. Exp Therm Fluid Sci. 2009;33(6):1012–20. doi:10.1016/j.expthermflusci.2009.05.002.
10. Bai B, Sun H, Zhang H, Liu L. Numerical study on turbulent mixing of spray droplets in crossflow. J Propuls Power. 2011;27(1):132–43. doi:10.2514/1.49826.
11. Zhang H, Bai B, Wang Y. Quantitative description of droplet dispersion of hollow cone spray in gaseous crossflow. Exp Therm Fluid Sci. 2018;93(4):398–408. doi:10.1016/j.expthermflusci.2018.01.023.
12. Tseng CC, Viskanta R. Effect of radiation absorption on fuel droplet evaporation. Combust Sci Technol. 2005;177(8):1511–42. doi:10.1080/00102200590956696.

13. Hashimoto N, Nomura H, Suzuki M, Matsumoto T, Nishida H, Ozawa Y. Evaporation characteristics of a palm methyl ester droplet at high ambient temperatures. Fuel. 2015;143:202–10. doi:10.1016/j.fuel.2014.11.057.
14. Tanvir S, Biswas S, Qiao L. Evaporation characteristics of ethanol droplets containing graphite nanoparticles under infrared radiation. Int J Heat Mass Transf. 2017;114:541–9. doi:10.1016/j.ijheatmasstransfer.2017.06.059.
15. Strizhak PA, Volkov RS, Antonov DV, Castanet G, Sazhin SS. Application of the laser induced phosphorescence method to the analysis of temperature distribution in heated and evaporating droplets. Int J Heat Mass Transf. 2020;163:120421. doi:10.1016/j.ijheatmasstransfer.2020.120421.
16. Antonov DV, Fedorenko RM, Strizhak PA, Sazhin SS. A simple model of heating and evaporation of droplets on a superhydrophobic surface. Int J Heat Mass Transf. 2023;201:123568. doi:10.1016/j.ijheatmasstransfer.2022.123568.
17. Beji T, Thielens M, Merci B. Assessment of heating and evaporation modelling based on single suspended water droplet experiments. Fire Saf J. 2019;106:124–35. doi:10.1016/j.firesaf.2019.04.012.
18. Sazhin SS. Advanced models of fuel droplet heating and evaporation. Prog Energy Combust Sci. 2006;32(2):162–214. doi:10.1016/j.pecs.2005.11.001.
19. Abramzon B, Sazhin S. Convective vaporization of a fuel droplet with thermal radiation absorption. Fuel. 2006;85(1):32–46. doi:10.1016/j.fuel.2005.02.027.
20. Jin ZC, Sun FX, Xia XL, Sun C. Numerical investigation of evaporation and radiation absorption of a non-spherical water droplet under asymmetrically radiative heating. Int J Heat Mass Transf. 2019;140(2):66–79. doi:10.1016/j.ijheatmasstransfer.2019.05.087.
21. Zhang P, Sun C, Sun F, Jin Z. Evaporation of single water droplet under laser irradiation. In: Proceedings of the International Heat Transfer Conference 16; 2018 Aug 10–15; Beijing, China. p. 787–99. doi:10.1615/ihtc16.bae.023566.
22. Godsave GAE. Studies of the combustion of drops in a fuel spray—the burning of single drops of fuel. Symp Int Combust. 1953;4(1):818–30. doi:10.1016/S0082-0784(53)80107-4.
23. Zhang D, Tu M, Yuan Y, Han W. Thermal radiative transfer characteristics of a single water droplet. Int J Heat Mass Transf. 2024;219:124824. doi:10.1016/j.ijheatmasstransfer.2023.124824.
24. Zhou WB, Yin JW, Zhang D, Yang Y, Yu JH, Zhao BC. Experimental study on the evaporation process of NaCl aqueous droplets under thermal radiation heating. CIESC J. 2024;75(S1):85–94. (In Chinese). doi:10.11949/0438-1157.20240337.
25. Zhang D, Zhou W, Liu S, Zhao B, Gao D, Zhang L. Study on evaporation characteristics of water droplet array under heating of thermal irradiation: monte Carlo method. Appl Therm Eng. 2025;262:125247. doi:10.1016/j.applthermaleng.2024.125247.
26. Palmer KF, Williams D. Optical properties of water in the near infrared. J Opt Soc Am. 1974;64(8):1107. doi:10.1364/josa.64.001107.
27. Correcher V, Garcia-Guinea J, Lopez-Arce P, Gomez-Ros JM. Luminescence emission spectra in the temperature range of the structural phase transitions of Na_2SO_4. Spectrochim Acta Part A Mol Biomol Spectrosc. 2004;60(7):1431–8. doi:10.1016/j.saa.2003.08.008.
28. Rudysh MY, Andriyevsky BV, Shchepanskyi PA, Karkulovska M, Stadnyk VY, Bychto L, et al. Optical refractive properties and phonon spectra of Na_2SO_4 single crystal. Opt Mater. 2025;166:117228. doi:10.1016/j.optmat.2025.117228.
29. Jia ZH. Research on evaporation characteristics of spherical droplet under infired laser heating [dissertation]. Harbin, China: Harbin Institute of Technology; 2016. Available from: https://kns.cnki.net/kcms2/article/abstract?v=FeJ59O1VQJclW6dXQlYLi_qPOt41w0lR6snWeLw81CEEjSf7kOpcnOpH3F5TlyzeLpfmMxcdtsSP2a7bd3VCAfYJybPeuonq7mgPR-lrkLrZ1T0qEj71fatHcpZhQzuGT3xrApmfaGtW5fFEJEpCLgCxJ5GXPxeVUp3gHflAphPwPAzfLxX_xkR5OvIdNtjt&uniplatform=NZKPT&language=CHS.
30. Moffat RJ. Contributions to the theory of single-sample uncertainty analysis. J Fluids Eng. 1982;104(2):250–8. doi:10.1115/1.3241818.